Book of Tutorials and Abstracts

European Microbeam Analysis Society

EMAS 2025

18th

EUROPEAN WORKSHOP

on

MODERN DEVELOPMENTS AND APPLICATIONS IN MICROBEAM ANALYSIS

11 to 15 May 2025
at the
TecnoCampus
Mataró (Barcelona), Spain

Organized in collaboration with the
Universitat de Barcelona, Spain

EMAS
European Microbeam Analysis Society eV
www.microbeamanalysis.eu/

This volume is published by:
European Microbeam Analysis Society eV (EMAS)
EMAS Secretariat
c/o Eidgenössische Technische Hochschule, Institut für Geochemie und Petrologie
Clausiusstrasse 25
8092 Zürich
Switzerland

ISBN 978 90 8227 6985
NUR code: 972 – Materials Science

PIXELS, PATTERNS, PSEUDOSYMMETRIES: ON RESOLUTION LIMITS OF EBSD

Aimo Winkelmann[1,2], G. Cios[1], K. Mehnert[2] and P. Bała[1]

1 AGH University of Krakow, Academic Centre for Materials and Nanotechnology (ACMiN)
Al. A. Mickiewicza 30, PL-30059 Krakow, Poland
2 ST-Development GmbH
Wilhelmshöhe 7, 33102 Paderborn, Germany
e-mail: winkelmann@agh.edu.pl

Aimo Winkelmann obtained his PhD in Physics in 2003 with a thesis entitled "Electron diffraction methods for structure analysis of epitaxial silicon carbide films". From 2004 to 2013 he worked at the Max-Planck-Institute of Microstructure Physics (Halle, Germany). In 2012 he obtained his Habilitation in Experimental Physics from the Martin-Luther-University Halle-Wittenberg (Germany), with a thesis entitled: “Nonlinear photoemission at metal surfaces under the influence of spin-orbit-coupling”. From 2013 to 2018 he was Senior Scientist EBSD at Bruker Nano GmbH (Berlin, Germany). He worked from 2018 and 2019 at the Laser Zentrum Hannover (Germany). Since 2015 he is Visiting Professor at the University of Strathclyde (Glasgow, Scotland) and since 2019 he is Associate Professor at the Academic Center for Materials and Nanotechnology (ACMiN) of AGH University of Krakow (Poland).

1. ABSTRACT

Electron backscatter diffraction (EBSD) is a widely used technique for the determination of crystal structure information, orientation, and strain data from Kikuchi diffraction patterns. Realistic pattern simulations play a key role in enhancing the resolution limits achievable by EBSD systems. We explore a super-sampling method for deriving high-resolution parameters from experimental Kikuchi diffraction patterns of varying resolutions. Within this framework, we consider the implications of factors like the precision of the projection centre and the impact of strain tensor element noise on the accuracy of strain-induced shape changes, and we emphasise utilising the normalised cross-correlation coefficient (NCCC) as an image similarity metric to reliably identify small symmetry-breaking effects in experimentally detected Kikuchi patterns.

2. INTRODUCTION

The analytical capability of EBSD systems that are available to scanning electron microscopy (SEM) lab users has steadily increased since the commercial introduction of the method and its development into one of the standard tools of SEM-based crystallographic microstructure analysis.

In order to quantify the performance of EBSD in terms of "resolution", we have, for example, aspects related to the underlying physical principles of scanning electron microscopy and to Kikuchi pattern formation in general and, on the other hand, problems of data analysis, i.e., how to best extract spatially resolved crystal structure information, orientations, and strain data from measured Kikuchi patterns. In this contribution, we focus on details of EBSD pattern data analysis approaches, while we refer the interested reader to comprehensive reviews and studies concerning the spatial and energy resolution of EBSD [1-3].

The angular resolution is a particularly crucial parameter in EBSD systems, as it determines the precision of the orientations acquired from experimental Kikuchi patterns through the data analysis method. Commercial EBSD systems are largely based on the use of the Hough transform [4] to detect linear features of the Kikuchi bands and to relate these to crystal orientations with a precision improving from approximately 1° in early systems [5] to resolutions well below 0.1° with improved methods that combine the Hough transform with additional information provided by the specific shape of Kikuchi diffraction bands [6-9]. As the pixel dimensions on the detected diffraction patterns are linked to angular ranges of scattering directions, it might be anticipated that an improvement in pixel resolution of the captured Kikuchi patterns will also improve the achievable angular resolution.

In the domain of pattern-based approaches, high-angular resolution EBSD (HR-EBSD) techniques are a powerful tool especially for analysing strain in materials due to their high sensitivity to small changes in crystal lattice parameters and orientations [10-12]. These methods

allow for the measurement of elastic strains with a sensitivity of approximately $\pm 2\times10^{-4}$ [11, 13] in the individual components of the infinitesimal strain tensor, making it suitable for studying a variety of phenomena, including residual stresses, strain fields around defects, and the behaviour of materials under load. HR-EBSD methods usually work best with diffraction patterns having resolutions in the order of 1,000×1,000 pixels or more [14].

One crucial tool for pattern matching-based EBSD is the use of realistic pattern simulations, which can significantly improve the resolution limits attainable with advanced EBSD systems. Studies on the use of Kikuchi pattern simulations focussed on achieving high-resolution orientation determination via pattern matching [15], tackling pseudosymmetry challenges [15-17], and presenting novel indexing techniques like dictionary indexing [18] and spherical indexing [19, 20]. These approaches prioritize varying levels of speed and precision. Dynamical simulations of Kikuchi patterns [21] are anticipated to play a crucial role in deriving high-resolution strains from experimental EBSD data. The theoretical feasibility of extracting strain tensors from EBSD data via simulations has been previously examined using numerical simulations of EBSD patterns [22-24]. Based on the theoretical assessment detailed in [24], the application of pattern matching utilising binned patterns with lower resolution than those typically employed in high-resolution EBSD applications could potentially facilitate a more data-efficient determination of strain tensors.

We recently demonstrated in [28] that a pattern matching approach based on simulated high-resolution patterns is able to closely reproduce results obtained previously for indentation experiments on Si from full resolution raw patterns (e.g., 1,244×1,024 in 16-bit resolution) by simulation-based super-sampling of significantly lower resolution patterns (e.g., 311×256) at 8-bit. This means that data storage requirements for the same experiment would be reduced by a factor of 32 in this example case (factors of 2 due to 16/8 bit, and 16 due to 4×4 binning). In the present contribution, we discuss additional details related to the performance of the super-resolution pattern matching approach presented in [28] with respect to the influence of the projection centre precision, the noise-related limits on the knowledge of shape change under strain, as well as the sensitivity of EBSD pattern matching to symmetry breaking using the example of handedness in quartz.

2.1. Simulation-based super-resolution pattern matching

In the pattern matching method discussed here, we use the term super-resolution to describe a method designed to infer high-resolution parameter output from low-resolution image input.

The principle of parameter-super-resolution EBSD pattern matching is explained in Fig. 1, where we argue that a high-resolution simulation can act as a fill-in model for the diffraction sub-structure to describe small changes within the binned, large pixels of a low-resolution pattern. In a sense, the binned pattern is a view of a higher-resolution pattern as seen behind frosted glass pane, and the high-resolution simulation can predict how a rotated and strained

pattern would look like when seen blurred through the glass. To control the amount of super-sampling in the implemented pattern matching method, one can choose a super-sampling parameter n_S which corresponds to a grid of $n_S \times n_S$ regular spaced theoretical sub-pixels inside of each experimental pixel area.

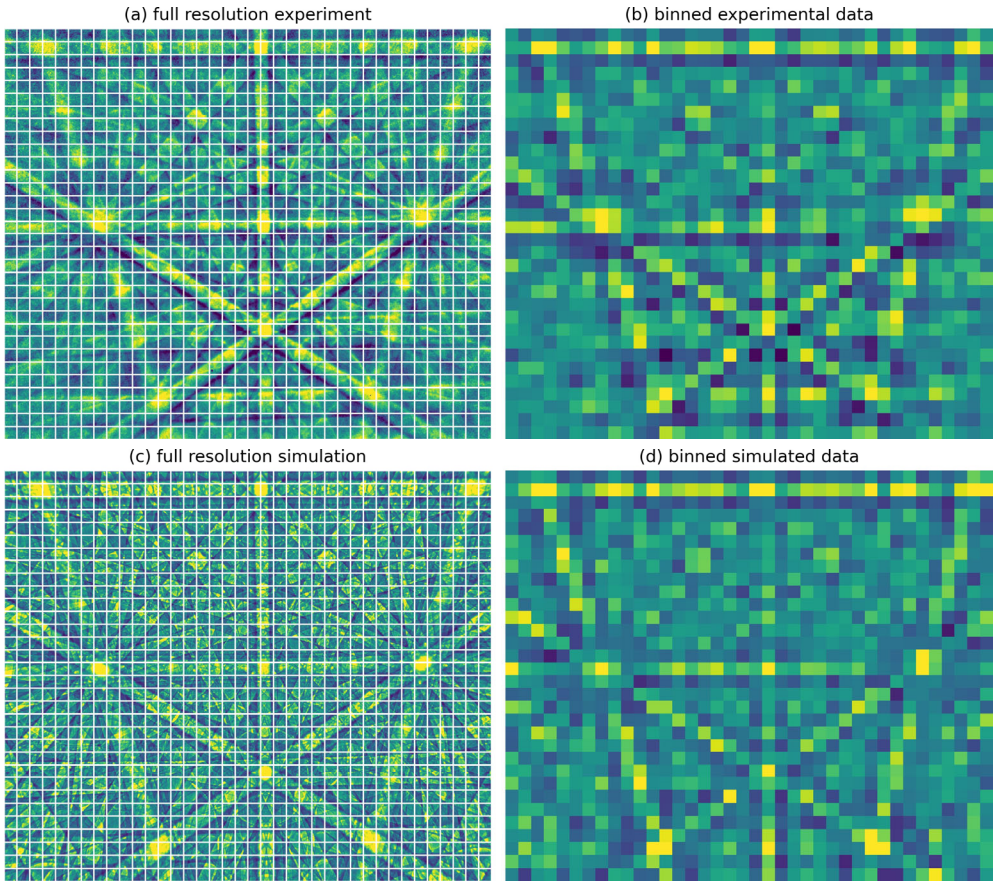

Figure 1. Principle of super-resolution Kikuchi pattern parameter fitting [28]. Simulated Kikuchi pattern data with 1,244×1,024 pixels on the detector area (c) is used to predict high-resolution parameter changes from 38×32 pixel-resolution experimental data (b) via comparison to consistently binned simulated data (d), thus circumventing the use of full-resolution 1,244×1,024 experimental data (a). The tolerable binning will depend on the required resolution of the fitted parameters.

The transformation of unit vector directions $[x_M, y_M, z_M]$ from a spherical master Kikuchi diffraction pattern to projected pixel centre coordinates $[p_1, p_2, p_3]$ on a planar screen can be understood as a projective transformation $\mathbf{F}$ acting on the homogeneous coordinates $[x_M, y_M, z_M]$ [23, 29, 30-35]:

$$\begin{bmatrix} p_1 \\ p_2 \\ p_3 \end{bmatrix} = \mathbf{F} \begin{bmatrix} x_M \\ y_M \\ z_M \end{bmatrix} = \boldsymbol{RU} \begin{bmatrix} x_M \\ y_M \\ z_M \end{bmatrix} \quad (1)$$

The coordinates (x_g, y_g) in the standard embedded projection plane at $z_g = 1$ are given by dehomogenisation of the projective coordinates as (x_g, y_g) = (p_1/p_3, p_2/p_3) for all projected points with $p_3 \neq 0$ [36]. The 3×3 matrix $\mathbf{F}$ has 8 degrees of freedom, because scaling of $\mathbf{F}$ by a real factor does not change the projective transformation [37].

As has been discussed by Maurice *et al.* [38, 39], Eq. (1) can also be seen as the definition of the deformation gradient tensor $\mathbf{F}$ with the polar decomposition $\mathbf{F} = \mathbf{RU} = \mathbf{VR}$ [40]. The right Biot stretch tensor $\mathbf{U}$ [41] describes the distortion in the sample system, while the left Biot stretch tensor $\mathbf{V} = \mathbf{RUR}^T$ can be used to describe the distortion in the rotated crystallophysical coordinate system.

The missing 9th degree of freedom for an overall scaling in the theoretical 3×3 model matrix $\mathbf{F}$ is consistent with the severely reduced experimental sensitivity of Kikuchi diffraction patterns to a small uniform expansion of the lattice relative to the changes of angles between crystallographic directions [42]. For the fitting approach that we use, we constrain $\mathbf{U}$ to be an isochoric transformation, that is, we prescribe a unit determinant for all the matrices involved, det $\mathbf{F}$ = det $\mathbf{R}$ = det $\mathbf{U}$ = 1, thereby having 8 free parameters in the 3×3 matrix $\mathbf{F}$.

The current EBSD pattern simulation models still have remaining limitations (especially related to the excess-deficiency effect [43]) that introduce severe biases in the strain results when the ideal simulated patterns (which lack some relevant experimental features) are directly compared to experimental ones. As discussed in [28], it should still be feasible to measure *relative* strains provided the bias remains nearly constant, such as in single crystal films or individual grains of polycrystalline samples. The relative strain then is determined with respect to reference points that can be assumed to be strain-free or which have a known deformation state.

The super-resolution method for high-resolution determination of orientations and relative deviatoric strain which we apply here is fully described in [28] and has been implemented in the AZTECCRYSTAL MAPSWEEPER software in Version 3.3 (Oxford Instruments).

3. *RESULTS AND DISCUSSION*

3.1. *Characterisation of shape changes under strain*

Tensor invariants provide important information that is independent of the chosen coordinate system. In [44] a set of invariants of the Hencky strain tensor $\boldsymbol{E}_H = \ln \boldsymbol{U}$ [41] has been suggested to characterise changes in size and shape of a material element that are caused by a strain tensor independently of the orientation of the cartesian axes.

Quantitative measures of distortion (= isochoric deformation) of a crystal unit volume can be constructed using a normalised deviator tensor $\mathbf{\Phi}$ [44]:

$$\mathbf{\Phi} = \mathrm{dev}\, \boldsymbol{E}_H / K_2 \tag{2}$$

where the invariant K_2 is defined using the Frobenius norm $||\ldots||_2$:

$$K_2 = ||\boldsymbol{E}_H||_2. \tag{3}$$

In this way, the Hencky strain tensor can be decomposed into $K_2 \geq 0$ which describes how much the shape of the unit volume changes, and $\mathbf{\Phi}$, which specifies how the shape change looks like:

$$\boldsymbol{E}_H = K_2\, \mathbf{\Phi}. \tag{4}$$

Moreover, the type of distortion can be numerically characterised by the scaled determinant K_3 of the normalised deviator $\mathbf{\Phi}$:

$$K_3 = 3\sqrt{6}\, \det \mathbf{\Phi}. \tag{5}$$

The invariant K_3 is in the range $[-1, 1]$, with the extreme cases $K_3 = 1$ for uniaxial extension (=equibiaxial contraction), $K_3 = -1$ for uniaxial contraction (=equibiaxial extension), and $K_3 = 0$ for pure shear strain, where one principal axis is not stretched at all and the other two principal axes are stretched and compressed in a reciprocal way [44].

For low strains approaching the noise level, the type of distortion inferred from the noisy strain tensor elements should also become random and the value of K_3 will then randomly vary from map point to map point, meaning that we are unsure about the actual type of shape change. This effect is qualitatively similar to the way the rotation axis becomes irrelevant for small rotation angles near the noise level in EBSD [45, 46].

In order to compare experimentally the various EBSD strain analysis methods, indents in Si wafers can serve as reproducible reference cases [25- 27]. As an example, in Fig. 2 we show the result of an indentation experiment on a silicon wafer sample, using different binning levels for the strain analysis.

At relatively high deformation magnitudes in the central area near the indent, as seen in the map of K_2, the corresponding map of K_3 indicates uniaxial compression in blue colour ($K_3 \approx -1$), which is consistent with the expectations of FEM simulations [28]. Moreover, at the tips of the cracks we see white spots that would indicate a pure shear distortion ($K_3 \approx 0$).

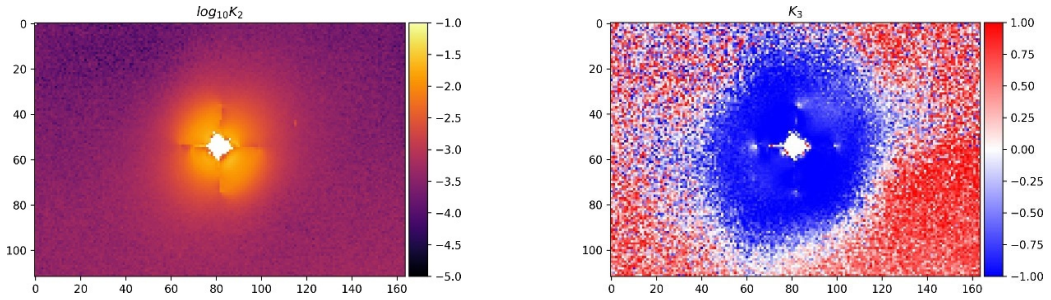

a) Pattern resolution 622×512 pixels, 7×7 simulation super-sampling

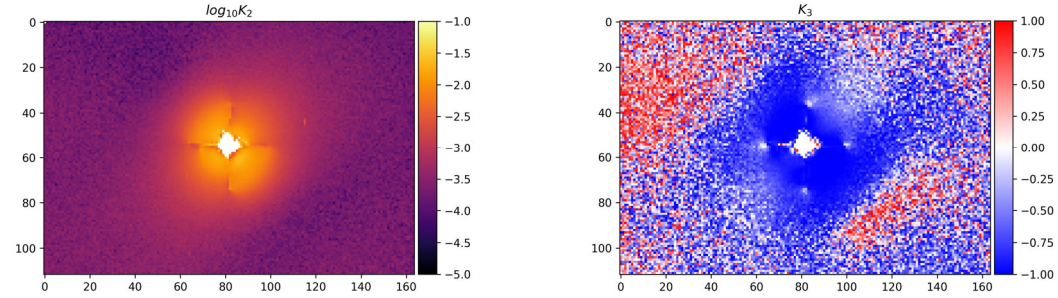

b) Pattern resolution 311×256 pixels, 13×13 simulation super-sampling

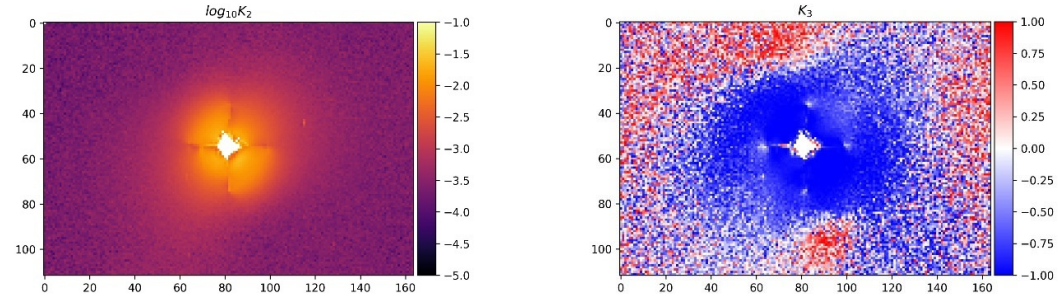

c) Pattern resolution 155×128 pixels, 25×25 simulation super-sampling

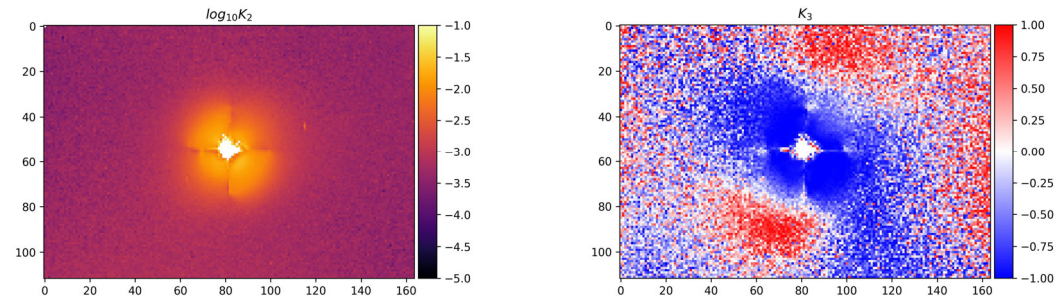

d) Pattern resolution 77×64 pixels, 49×49 simulation super-sampling

Figure 2. Relative isochoric strain near an indent on a Si(110) sample. Left column: Logarithm of the deviator norm K_2, right column: Distortion type K_3. ESBD analysis conditions: 20 kV, step size 1µm. The reference point for the relative strain values is at (0,0).

At lower levels of K_2 outside the immediate indent area, we see how K_3 becomes less well defined, as seen by more colour noise in red, white, and blue. Apparently completely random colour noise is seen in the nominally strain-free area near the reference point (0,0) on the upper left of the map, where the K_2 values also achieve their best minimum values in the range of a few 10^{-4} and below. With increasing distance away from the reference point, there are larger systematic red or blue areas in the K_3 maps, which we interpret is due to a slight remaining bias in the pattern fitting method. We assume that inherent limitations of the applied pattern matching projection centre calibration method [36] are causing systematic small phantom strains at large distances from the reference point. This can also be seen by slightly changing values of K_2 in the nominally strain-free area of the parts of the maps further away from the reference point. Ideally, in the strain-free regions, a completely unbiased strain analysis method should measure random strain tensor elements within the noise level of the method and this should lead to uniform red-white-blue noise in all of the strain-free regions. One might thus envision utilising the combination of K_2 and K_3 maps from a wide-area scan of a strain-free silicon sample as a comparison tool to verify any large-distance biases within a strain measurement technique.

Concerning the pattern resolution-dependence of the results shown in Fig. 2, we see that binning from 622×512 to 311×256 leads to a visually a very similar result, except for the exact distributions of K_3 in the strain-free areas. The results begin to clearly deteriorate from 155×128 to 77×64 pixels resolution, where one can visually detect the appearance of a larger noise floor in the K_2 signal of the strain-free areas. Analysing neighbour-pair differences for quantitative noise estimation, we found in [28] that the estimated standard deviation of the strain norm noise remains below 10^{-4} for patterns with resolutions down to 155×128 and 13×13 super-sampling.

The analysis of the K_2 maps shown in Fig. 2 in combination with the corresponding K_3 data indicates that for strain norm noise in the order of 0.1 mm/m (10^{-4}), the specific type of distortion becomes undetermined already for strain norms of about 1 mm/m (10^{-3}) (i.e., by estimating which levels of the K_2 map correspond to the boundary between the smooth blue area of the K_3 map near the indent and the noisy areas further out). This observation implies that we can know the total overall magnitude of a small strain much better than the actual resulting type of shape change, which becomes unreliable already at strain norms which are about one magnitude higher than the noise limit.

3.2. Projection centre calibration and strain sensitivity

To investigate in more detail the theoretical strain sensitivity of the super- resolution pattern matching method [28], which might be achievable without excess-deficiency features observed in the experiment, we examined simulated ideal pattern data from a theoretical polycrystalline sample consisting of about 50 different randomly oriented grains. In this analysis, the strain varies horizontally across the map from the left (x = 0.0) to the right (x = 1.0) and is described by a strain tensor $\boldsymbol{\varepsilon}(x)$ with ε_{max} = 1 mm/m and x = 0…1 as follows:

$$\boldsymbol{\varepsilon}(x) = \mathrm{x} * \begin{pmatrix} -\varepsilon_{max} & 0 & -\varepsilon_{max} \\ 0 & -\varepsilon_{max} & -\varepsilon_{max} \\ -\varepsilon_{max} & -\varepsilon_{max} & 2\varepsilon_{max} \end{pmatrix}. \quad (6)$$

This strain state is representative for a distortion type near uniaxial extension ($K_3 \approx 1.0$), independently of the strain magnitude. The resolution of the simulated patterns in the map was 311×256 and the beam energy was 20 kV. We assumed that the sample surface plane and the detector plane were parallel, because this setting allows us to show the implications of an incorrect projection centre calibration for the development of phantom strains and a phantom absence of strains. The synthetic map data was saved in the HDF$_5$-based H$_5$OINA format [47], and includes 10 scan lines of strain-free areas at the top and bottom, which are used to calibrate the projection centre on known strain-free points. The synthetic pattern data is analysed using the AZTECCRYSTAL MAPSWEEPER software Version 3.3 (Oxford Instruments), using exactly the same procedures as with experimentally acquired data. The H$_5$OINA data file is available at DOI 10.5281/zenodo.15050850 for download.

Figure 3 shows the result of the analysis when we correctly use map points in the strain-free area itself to calibrate the projection centre. The recovered strain values correspond to the prescribed theoretical values within numerical errors, which should be expected from an analysis that uses the same simulated model data for the emulation of the experiment and for its analysis. We note the random colour noise in the two strain free regions of the K_3 map, which indicates the absence of a significant systematic bias for the analysis of perfect simulated data.

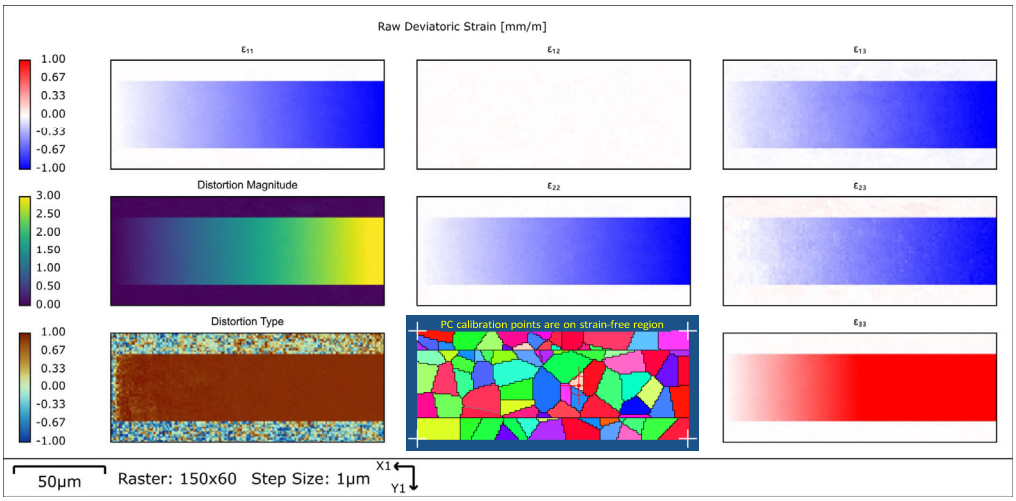

Figure 3. Simulated strain data according to Eq. (6), showing a gradient in the distortion magnitude, and a constant distortion type near uniaxial extension ($K_3 \approx 1.0$). $\varepsilon_{12} = \varepsilon_{21} = 0.0$. Distortion magnitude = K_2 (Eq. 3) in mm/m, distortion type = K_3 (Eq. 5, dimensionless).

Figure 4 shows the result of the analysis when we use map points on the strained area itself for the calibration of the projection centre. The result is a practically complete absence of any measured strain in the known strained region. Instead, a complementary phantom strain is measured in the non-strained region. The cancellation of strain in the strained region and the appearance of an opposite strain in the strain-free stripes can be understood from the structure of the prescribed strain tensor and how a changing projection centre would be described in the framework of Eq. (1).

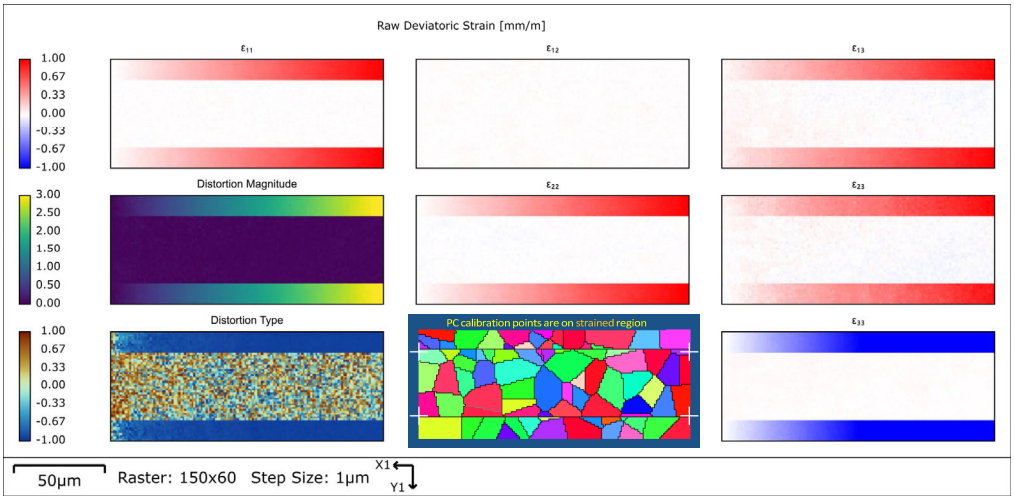

Figure 4. Same analysis as in Fig. 3, but wrongly calibrating on the strained region on the sample. This shows a practically complete absence of any measured strain in the strained region and a complementary phantom strain in the non-strained region.

Because we have the sample plane and the detector screen plane parallel, the ratios of the strain tensor elements $\varepsilon_{11}/\varepsilon_{33}$ and $\varepsilon_{22}/\varepsilon_{33}$ would correspond to changes of the z-coordinate of the projection centre (”zooming in or out of the pattern”), while the strain tensor off-diagonal elements ε_{13} and ε_{23} would be equivalent to a linear translation of the projection centre x, y-coordinates [48]. The effects of the strain tensor (6) on a projected pattern can thus be exactly mimicked by a moving projection centre during a scan, under the special conditions we were setting artificially. In a real experiment, this behaviour will be modified by the tilt of the surface plane, but qualitatively it remains that calibration of a scan on strained regions will lead to systematic errors in the strain measurement.

The only strain component that is exempt from the problem of projection centre calibration in the present case should be ε_{12}, because we can neglect any shearing of the rigid detector screen plane. That is why the condition of $\varepsilon_{12} = 0$ in the simulated strain tensor can be used as a test of how well the strain analysis approach recovers this condition. Figure 5 shows that our analysis approach results in a mean value near 3×10^{-6} (i.e., a minimal positive bias) with a standard

deviation near 1×10^{-5} on ideal, simulated data using a calibrated projection centre (fixed in the optimisation). This allows us to confirm that the numerical precision of the approach is well below the typically observed noise levels in real experiments.

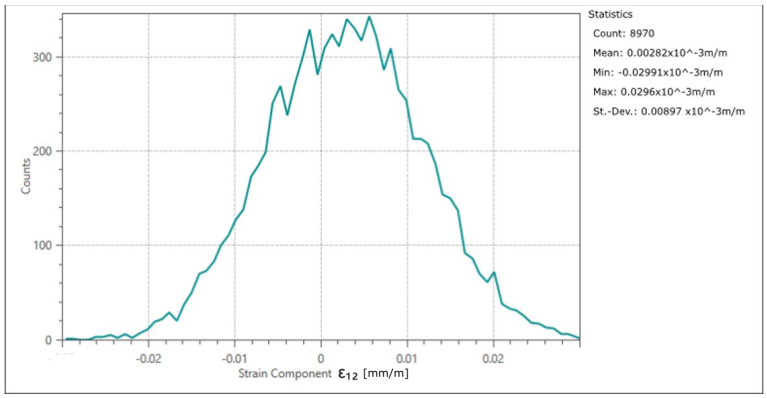

Figure 5. Distribution of the ε_{12} component of the analysed simulated strain data, with a true theoretical value of 0.0 underlying the pattern simulation.

In [24] it has been shown using ideal simulated data how a simultaneous determination of projection centre and deformation tensor severely degrades precision. The observed drop from basic machine precision 10^{-8} under ideal numerical conditions to 10^{-4} reflects the fact that the simultaneous fit of projection centre and deformation (which in general includes both rotation and strain) is poorly conditioned, as has been argued by Alkorta *et al.* [48]. In [49] it was found that the extraction of the deformation state based on simulated patterns showed a mean accuracy of 1×10^{-3} in the shear components and about 2×10^{-3} in the diagonal components (normal strains) when optimising while including the projection centre in the fit. This approach was also applied in [49] to experimental data in a hybrid approach that fits the reference point strain state based on simulated data and then measures the relative strains with a conventional cross-correlation based approach between experimental reference and experimental data patterns. Correcting the relative experimental strains by the simulation-based reference strains, partially more consistent strain states were observed in the shear component ϵ_{12}, while the agreement in the other components was less good. These observations are in qualitative agreement with our discussion related to ε_{12} in the present case. Because of the equivalence of a changing projection centre and a developing strain as seen by a projected Kikuchi pattern, our simulation-based analysis above emphasises the need for a precise, independent, calibration of the beam position relative to the detector with a relative error below the desired strain resolution for absolute strain determination, because the resulting errors would appear even if the simulated Kikuchi pattern would match practically perfectly to the experiment.

3.3. Symmetry breaking

The action of strain on a crystalline sample can be interpreted as a local change of the crystal unit cell, i.e., a general strain in a cubic crystal will reduce the abstract, mathematical symmetry to triclinic. However, this apparently drastic symmetry-breaking from cubic to triclinic is not necessarily reflected by a similarly drastic change in the diffraction pattern. Instead, the observed Kikuchi pattern remains closely similar to the unstrained one, with hardly any observable changes for small strains. In this sense, strain is an example for symmetry breaking and the exact discrimination of small strains deviating from a cubic structure is related to similar pseudosymmetry problems as the discrimination of two different crystal structures that lead to very similar Kikuchi diffraction patterns. In both cases, it is important to quantify the sensitivity of the measured Kikuchi patterns to the expected changes of the unit cell.

As an example for a challenging pseudosymmetry problem in ESBD, we use the example of the discrimination of the handedness of quartz, where the expected changes in the Kikuchi pattern between the left-handed and the right-handed modification are very small. This is because the crystal lattice parameters of both structures are exactly the same and only the chiral sense of arrangement of the unit cell atoms changes [50]. In [50] it was demonstrated that the discrimination of quartz chirality is possible from single-crystal samples of known handedness by comparison of the experimental patterns to dynamical simulations which are sensitive to the breaking of Friedel's law by non-centrosymmetric structures. The EBSD mapping of a locally changing quartz chirality and the identification of characteristic domain patterns in agate has been demonstrated in [51].

In Fig. 6, we show the effects of a pattern comparison between an experimental quartz pattern and the two possible simulations for left-handed and right-handed quartz, respectively. The pattern resolution is 156×128, and the pattern was measured at 15 kV beam voltage.

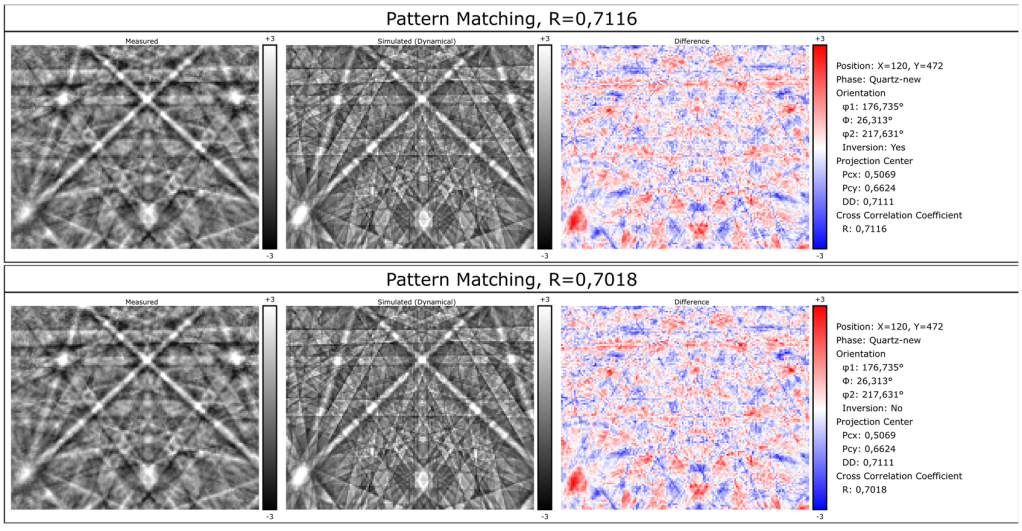

Figure 6. Change of the normalised cross-correlation coefficient for simulations corresponding to inverted crystal structures of quartz. The two theoretical patterns show R = 0.974.

For the quantitative comparison of the Kikuchi patterns, we apply the normalised cross-correlation coefficient (NCCC) R to measure the similarity of two EBSD patterns [52, 53]. It can be argued that the normalised cross-correlation coefficient is a much more reliable and sensitive image similarity metric for comparison of very similar Kikuchi patterns than the ”Normalised Dot Product” (NDP) metric [18], which also continues to be discussed as a similarity measure for EBSD pattern matching. The main advantage of the NCCC is that it is intrinsically insensitive to the actual brightness and contrast of the patterns that are compared, while the NDP is not. Moreover, while both metrics give a value of 1.0 for comparison of a pattern with itself, the NCCC also produces consistent reference values near 0.0 for comparisons of Kikuchi patterns to random noise, as well as for comparisons of noise to noise, with a theoretical mean value of 0.0 in both cases. The NDP, in contrast, does not give values near 0.0 for a comparison of random noise to random noise, but a value near 0.75 (theoretical value 3/4) and in general it also gives a significantly different value than 0.75 for pattern-to-noise comparison depending on the brightness and contrast of the non-noise pattern [54]. It might be considered to be desirable that the similarity metric for an EBSD pattern compared to noise should at least not indicate a significantly better or worse fit than a comparison of noise to noise. The underlying reason for this undesirable bias of the NDP is that the images are normalised to the range 0.0 - 1.0 when calculating the NDP, and thus low-intensity pixels are considered less important by the NDP whereas high-intensity pixels are preferentially emphasised. Additionally, in the presence of noise, even the location of the minimum values “0.0” and maximum values “1.0” in a pattern will change and influence the NDP. Conversely, the NCCC accurately accounts for the fact that, within a Kikuchi diffraction pattern, both high-intensity and low-intensity pixels hold equally significant information. The pixels which form black lines are just as crucial as those that form the white lines in a Kikuchi pattern, meaning we should focus on local deviations from the mean intensity within a Kikuchi pattern, not on the absolute intensity itself. This is evident from the NCCC’s computation, which is based on patterns normalised to have a zero mean and a standard deviation of one [54]. The characteristics of the NCCC are particularly advantageous when the difference between two potential solutions are minimal and it is essential to avoid any bias introduced by the metric used for pattern comparison.

Concerning the comparison shown in Fig. 6, we find that the NCCC is $R = 0.7116$ for the best fit pattern compared to $R = 0.7018$ for the alternative. In the present case, this means that the winning solution is the one for the inverted “left-handed” structure relative to the “right-handed” one that was used for the simulation. The observed change of $\Delta R = 0.01$ between the two possibilities may appear small but is statistically significant, as discussed in [55]. As a general rule for typical Kikuchi patterns measured in EBSD, changes of $\Delta R = 0.01$ at mean values of $R > 0.5$ can be assigned to true differences in the simulations, and the probability that such changes can be caused, for example, by noise in the experimental pattern, can be neglected. The difference ΔR between the two simulated patterns is $R = 0.974$, i.e., a drop of only $\Delta = 0.026$ would be observed even if we would measure ideal theoretical patterns, with the correct pattern simulation fitting perfectly with $R = 1.0$. Scaled to real experimental applications, we estimate that theoretical correlation coefficients near 0.98 and below are useful indicators for

experimentally possible discrimination of two related pseudosymmetric variants, provided that the quality of the experimental pattern is good enough to lead to large enough correlation coefficients between experiment and theory [55]. As an example of a complex pseudosymmetry problem that can be solved using the pattern matching approach we refer the reader to [17], where the distribution of six pseudosymmetric variants in Cu_6Sn_5 has been demonstrated.

4. SUMMARY AND OUTLOOK

We have discussed advancements in electron backscatter diffraction emphasising improvements in pattern data analysis by using a super-sampling approach based on high-resolution simulations in combination with Kikuchi patterns of varying experimental resolutions.

A significant challenge for future improvements of the EBSD pattern matching pipeline remains the efficient treatment of the excess-deficiency effect. This issue currently limits the achievable accuracy of simulation-based strain determination and projection centre calibration [43].

6. REFERENCES

[1] Engler O, Zaefferer S and Randle V 2024 Introduction to texture analysis. [Boca Raton, FL: CRC Press]
[2] Steinmetz D R and Zaefferer S 2010 *Mater. Sci. Technol.* **26** 640-645
[3] Winkelmann A, Britton T B and Nolze G 2019 *Phys. Rev. B* **99** 064115
[4] Krieger Lasssen N C 1994 *Automated determination of crystal orientations from electron backscattering patterns*. PhD thesis. [Kongens Lyngby, Denmark: Technical University of Denmark]. https://www2.imm.dtu.dk/pubdb/pubs/1200-full.html
[5] Humphreys F J 1999 *J. Microscopy* **195** 170-185
[6] Thomsen K, Schmidt N H, Bewick A, Larsen K and Goulden J 2013 *Microsc. Microanal.* **19** (Suppl. 2) 724-725
[7] Wright S, Nowell M and Basinger J 2011 *Microsc. Microanal.* **17** (Suppl. 2) 406-407
[8] Kacher J, Landon C, Adams B L and Fullwood D 2009 *Ultramicroscopy* **109** 1148-1156
[9] Brough I, Bate P S and Humphreys F J 2006 *Mater. Sci. Technol.* **22** 612-617
[10] Troost K Z, van der Sluis P and Gravesteijn D J 1993 *Appl. Phys. Lett.* **62** 1110-1112
[11] Wilkinson A J, Meaden G and Dingley D J 2006 *Ultramicroscopy* **106** 307-313
[12] Wright S I, Nowell M N and Field D P 2011 *Microsc. Microanal.* **17** 316-329
[13] Edwards T E J, Maeder X, Ast J, Berger L and Michler J 2022 *Sci. Advances* **8** abo5735
[14] Dingley D J, Meaden G, Dingley D J and Day A P 2018 *IOP Conf. Ser.: Mater. Sci. Eng.* **375** 012003
[15] Winkelmann A, Jablon B M, Tong V S, Trager-Cowan C and Mingard K P 2020 *J. Microscopy* **277** 79-92

[16] Burkhardt U, Winkelmann A, Borrmann H, Dumitriu A, König M, Cios G and Grin Y 2021 *Sci. Advances* **7** eabg0868
[17] Martin S, Winkelmann A and Leineweber A 2022 *Acta Materialia* **229** 117828
[18] Chen Y H, Park S U, Wei D, Newstadt G, Jackson M A, Simmons J P, De Graef M and Hero A O 2015 *Microsc. Microanal.* **21** 739-752
[19] Hielscher R, Bartel F and Britton T B 2019 *Ultramicroscopy* **207** 112836
[20] Lenthe W C, Singh S and De Graef M 2019 *Ultramicroscopy* **207** 112841
[21] Winkelmann A, Trager-Cowan C, Sweeney F, Day A P and Parbrook P 2007 *Ultramicroscopy* **107** 414-421
[22] Fullwood D, Vaudin M, Daniels C, Ruggles T and Wright S I 2015 *Mater. Characteriz.* **107** 270-277
[23] Ruggles T J, Bomarito G F, Qiu R L and Hochhalter J D 2018 *Ultramicroscopy* **195** 85-92
[24] Kurniawan C, Zhu C and De Graef M 2021 *Scripta Materialia* **190**) 147-152
[25] Wilkinson A J and Britton T NB 2012 *Mater. Today* **15** 366-376
[26] Britton T B, Jiang J, Clough R, Tarleton E, Kirkland A I and Wilkinson A J 2013 *Ultramicroscopy* **135** 136-141
[27] Koko A, Marrow J and Elmukashfi E 2021 arXiv:2107.10330
[28] Winkelmann A, Cios G, Perzyński K, Tokarski T, Mehnert K, Madej Ł and Bała P 2025 arXiv:2502.11628
[29] Alkorta J, Marteleur M and Jacques P J 2017 *Ultramicroscopy* **182** 17-27
[30] Winkelmann A, Nolze G, Cios G and Tokarski T 2018 *Phys. Rev. Mater.* **2** 123803
[31] Ernould C, Beausir B, Fundenberger J-J, Taupin V and Bouzy E 2020 *Acta Materialia* **191** 131-148
[32] Ernould C, Beausir B, Fundenberger J-J, Taupin V and Bouzy E 2022 *Development of a homography-based global DIC approach for high-angular resolution in the SEM*. in: Advances in imaging and electron physics. [Amsterdam, The Netherlands: Elsevier] 49-73
[33] Shi Q, Loisnard D, Dan C, Zhang F, Zhong H, Li H, Li Y, Chen Z, Wang H and Roux S 2021 *Mater. Characteriz.* **178** 111206
[34] Shi Q, Plancher E, Loisnard D, Karamched P, Liu J, Chen Z, Wang H and Roux S 2022 *Mater. Characteriz.* **194** 112458
[35] Shi Q, Zhong H, Loisnard D, Nowell M, Mollens M, Chen Z, Wang H and Roux S 2024 *Mater. Characteriz.* **218** 114508
[36] Winkelmann A, Nolze G, Cios G, Tokarski T and Bała P 2020 *Materials* **13** 2816
[37] Hartley R and Zisserman A 2003 *Multiple view geometry in computer vision*. [Cambridge, UK: Cambridge University Press]
[38] Maurice C, Driver J H and Fortunier R 2012 *Ultramicroscopy* **113** 171-181
[39] Maurice C, Plancher E and Klöcker H 2014 *A novel finite strain framework for HR-EBSD*. RMS UK EBSD Meeting.
[40] Reddy J N 2013 *An introduction to continuum mechanics. 2nd Edition*. [Cambridge, UK: Cambridge University Press]
[41] Neff P, Eidel B and Martin R J 2016 *Arch. Rat. Mechanics Analys.* **222** 507-572

[42] Villert S, Maurice C, Wyon C and Fortunier R 2009 *J. Microscopy* **233** 290-301
[43] Winkelmann A, Nolze G, Cios G, Tokarski T, Bała P, Hourahine B and Trager-Cowan C 2021 *J. Microscopy* **284** 157-184
[44] Criscione J C, Humphrey J D, Douglas A S and Hunter W C 2000 *J. Mechanics Phys. Solids* **48** 2445-2465
[45] Prior D J 1999 *J. Microscopy* **195** 217-225
[46] Bate P S, Knutsen R D, Brough I and Humphreys F J 2005 *J. Microscopy* **220** 36-46
[47] Oxford Instruments NanoAnalysis HDF5 File Specification https://github.com/oinanoanalysis/h5oina/blob/master/H5OINAFile.md (Accessed November 23, 2024)
[48] Alkorta J 2013 *Ultramicroscopy* **131** 33-38
[49] Zhu C, Kurniawan C, Ochsendorf M, An D, Zaefferer S and De Graef M 2022 *Ultramicroscopy* **233** 113407
[50] Winkelmann A and Nolze G 2015 *Ultramicroscopy* **149** 58-63
[51] Cios G, Winkelmann A, Tokarski T and Bała P 2025 arXiv:2501.08901
[52] Tao X and Eades A 2005 *Microsc. Microanal.* **11** 341-353
[53] Winkelmann A, Nolze G, Vos M, Salvat-Pujol F and Werner W S M 2016 *IOP Conf. Ser.: Mater. Sci. Eng.* **109** 012018
[54] Winkelmann A 2018 , xcdskd: Tools and methods for Kikuchi diffraction. https://xcdskd.readthedocs.io/en/latest/cross_correlation/cross_correlation_coefficient.html
[55] Burkhardt U, Borrmann H, Moll P, Schmidt M, Grin Y and Winkelmann A 2020 *Sci. Reports* **10** 4065